The magnetic permeability signature in high-frequency electromagnetic data modeling: a case study for GPR approximation

Alejandra I. Sánchez* and Luis A. Gallardo

Department of Applied Geophysics, Centro de Investigación Científica y de Educación Superior de Ensenada (CICESE), Ensenada, Mexico

Ground penetrating Radar (GPR) is a high-frequency geophysical prospecting method whose signal is affected by dielectric permittivity (ε), electrical conductivity (σ) and magnetic permeability (μ), but it is common practice to assume that magnetic permeability has a negligible influence on electromagnetic (EM) fields in geophysical applications. In this paper, we analyze the distinctive effect of magnetic permeability on the radar signal. To evaluate the transit of an electromagnetic wave, we developed a finite-difference time-domain (FDTD) algorithm that accounts for $\varepsilon-$, $\mu-$, and $\sigma-$ heterogeneities. Using a hypothetical coupled-layer model and an archaeological test example, we demonstrate the importance of considering magnetic permeability in numerical EM modeling, concluding that magnetic permeability is as relevant as the other property variations and also is the only property that simultaneously affects the velocity and attenuation of the electromagnetic wave and produces a unique energy partition unpredicted by any combination of the other two EM properties.

1 Introduction

Ground penetrating Radar (GPR) is a non-invasive, high-resolution and highly versatile geophysical prospecting method with diverse applications. The range of radar applications is vast due to their high frequency signal and the wide range of electromagnetic property variations. It is commonly used in geotechnical studies to locate pipes and to determine concrete and pavement conditions in buildings and paved-roads (Cassidy et al., 2011; Zhou and Zhu, 2021), to identify buried objects in forensic geophysics (Schultz and Martin, 2012; Aditama et al., 2015), to locate mines and unexploded ordnances (Steven et al., 2010; Giannakis et al., 2016), in studies of glaciers and permafrost (Hamran et al., 1998; Woodward and Burke, 2007), and to monitor water content in rocks (Klotzsche et al., 2018; Zhou et al., 2019). It is also common to combine the GPR studies with other geophysical or teledetection techniques. For example, to
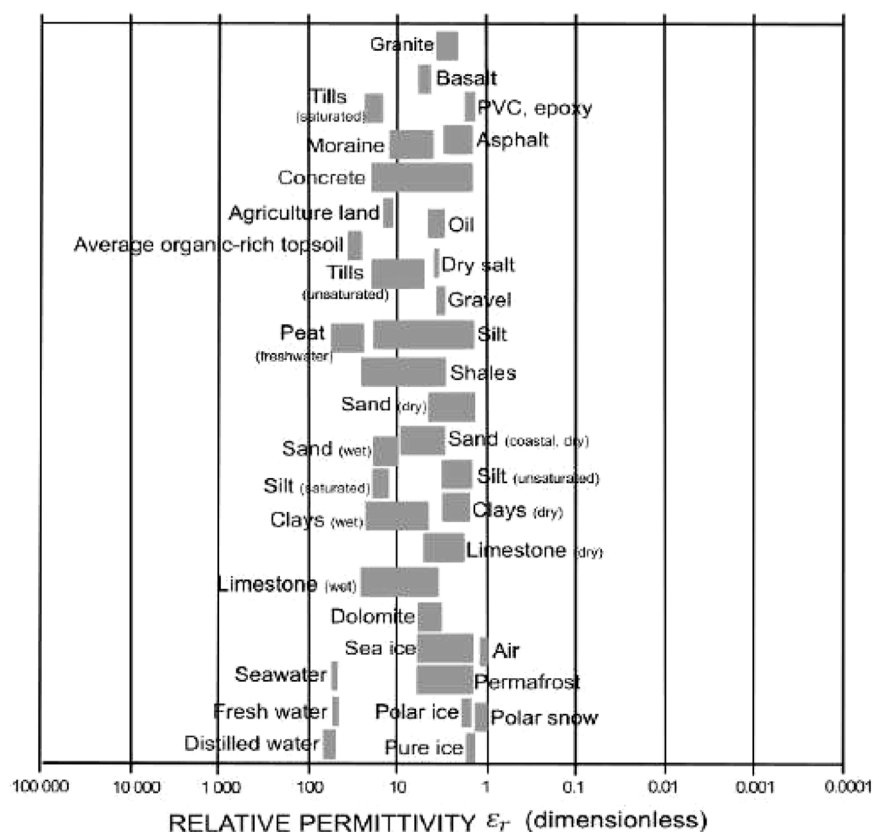
FIGURE 1
Ranges of relative permittivity values for various materials. Data combined from the compilations of Butler (2012), Reynolds (2011) and Reichard (2020). Note the coincidence of the permittivity values for most materials and that values lie within two orders of magnitude.

detect deformation zones or subsidence areas (Alonso-Díaz et al., 2023; La Bruna et al., 2024) or in forensic studies (Berezowski et al., 2024; Molina et al., 2024), among other applications.

In archaeology in particular, it is commonly used alone or in combination with other geophysical techniques to search for buried remains, mounds, settlement patterns and ancient buildings (Conyers et al., 2019; Ortega-Ramírez et al., 2020). For instance, coincidences have been found in the results of magnetic exploration and GPR, as in the work of Bianco et al. (2024), who demonstrated the advantages of an integrated interpretation of magnetic and GPR data in archaeological structures. This implies that a magnetic signature exists in both data types, but the underlying magnetic signature in radar data is poorly studied.

It is noticeable that, even in low-frequency electromagnetic (EM) signals, some studies address the importance of magnetic permeability. Pavlov and Zhdanov (2001) analysed the influence of magnetic permeability in TDEM surveys. Noh et al. (2016) evaluated the effects of conductivity and magnetic permeability in the frequency domain controlled-source EM methods. Xiao et al. (2022) studied the resistivity and magnetic susceptibility responses for a 3D Controlled-source audio-frequency magnetotellurics modeling. Heagy and Oldenburg (2023) considered how magnetic permeability contributes to the EM response of a cased well in grounded source EM experiments. Qiao et al. (2025) analysed

numerical experiments for a marine magnetotelluric approach considering variations in conductivity and magnetic permeability for 3D modeling. Notably, all of them concluded that the magnetic permeability influences the EM signal.

By being the highest frequency EM technique, it seems reasonable that the three properties must also be considered in radar data. Some authors have studied the effect of μ on radar signal transmission. Olhoeft (1998) demonstrated the importance of electrical, magnetic and geometric properties in radar electromagnetic modeling. Lazaro-Mancilla and Gómez-Treviño (2000) considered variations in the three electromagnetic properties in horizontal layers in the frequency domain and used propagation matrices to obtain the surface electric field. Pettinelli et al. (2007) analyzed the effect of electrical and magnetic properties on wave attenuation for different scenarios of the Martian surface. Cassidy (2008) investigated the attenuation and propagation characteristics of GPR signal for a range of nano-to-micro scale quartz/magnetite mineral mixtures. He determined that even with relatively low amounts of magnetite, the magnetic materials can considerably affect signal attenuation. Persico et al. (2012) used 3-D experimental data and a two-dimensional Born approximation to explore the influence of dielectric and magnetic properties on the radar signal. They pointed to an interesting relationship between permittivity and permeability. In a laboratory experiment, Van Dam et al. (2013) described the effect of magnetite on the radar signal, and they
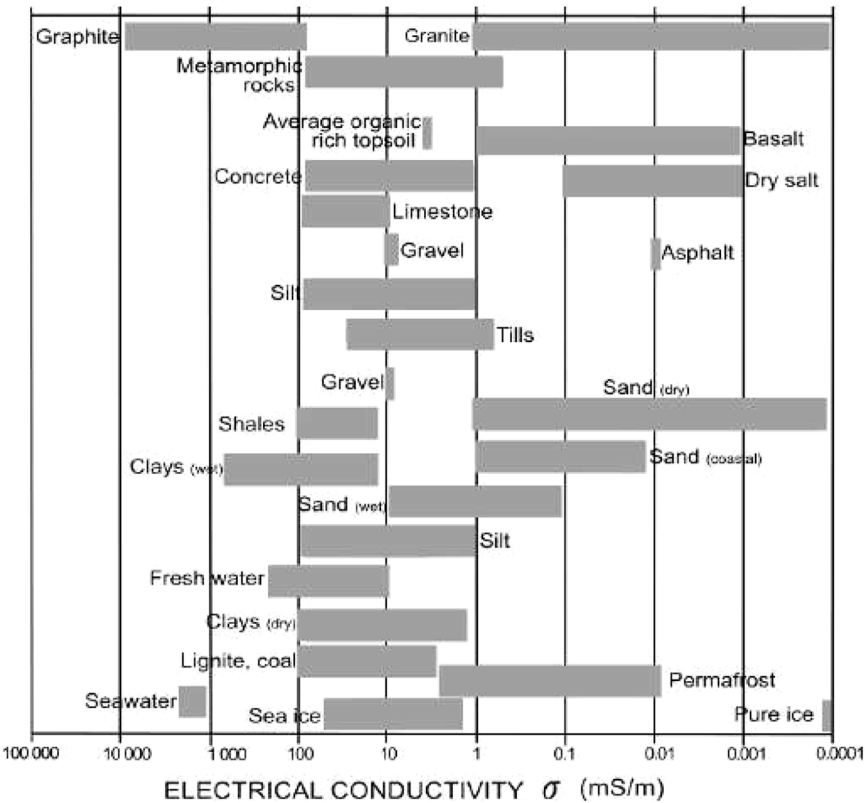
FIGURE 2
Ranges of electrical conductivity (adapted from Palacky (2012). Note the wide range (eight orders of magnitude) of the conductivity and the significant conductivity variations for individual materials depending on specific material conditions.
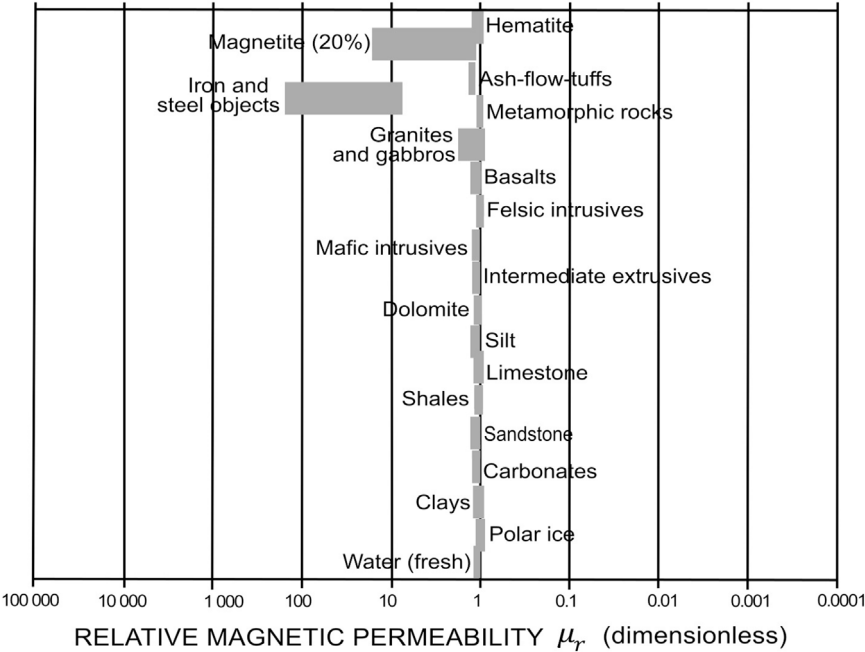
FIGURE 3
Ranges of relative magnetic permeability adapted from Palacky (2012) and Reichard (2020). Note the three orders of magnitude variations and the marked dominant groups identified as magnetic and non-magnetic.

FIGURE 4
FDTD Yee distribution for a single 3D cell (left) showing the electric (blue) and magnetic (orange) field components. Individual elements for TM and TE modes are shown in the right panel.

concluded that the magnetite significantly reduces the speed of radar waves. As in the EM low frequency signals, these authors concluded that the magnetic permeability influences various characteristics of the GPR signal.

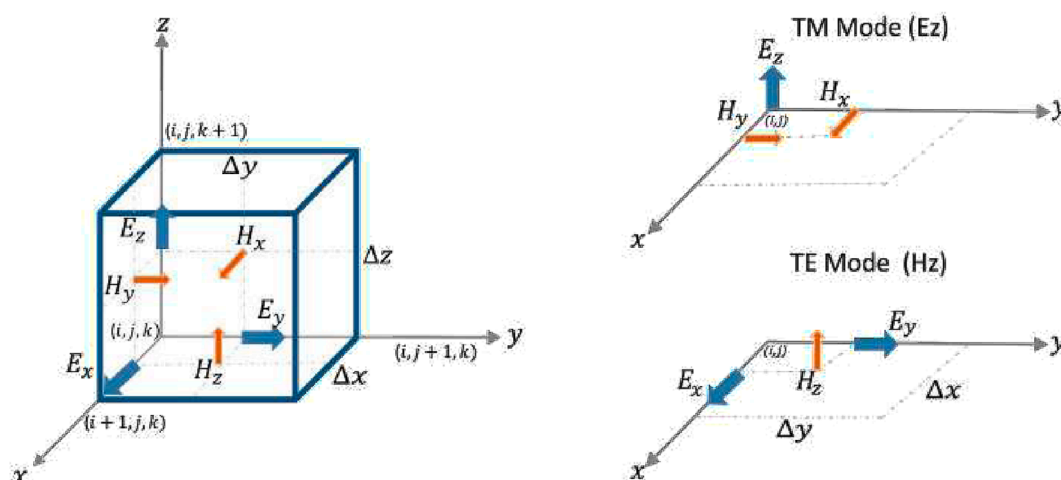Although the effect of ferromagnetic materials in the GPR signal has been studied, it is still unclear whether this signal is individually distinguishable from those produced by dielectric permittivity and electrical conductivity or not. It is also arguable if magnetic permeability contrast could significantly influence radar signals so as to be noticeable in geophysical data modeling and, ultimately, whether we should be able to infer this magnetic permeability contrast in an inverse problem. We posit that magnetic permeability does affect the observations differently from either electric permittivity or conductivity contrasts and should thus be considered in radar signal modeling and inversion.

This paper analyses the separate and combined influence of the three electromagnetic properties in EM wave propagation at the frequency range of radar signals. The finite-difference time-domain (FDTD) method was implemented to compute the EM response. We compare the computed fields with those from the widely used software gprMax (Giannopoulos, 2005; Warren et al., 2016). We then test if the electromagnetic response of the three properties can be individually distinguished in its propagation through the different media or in its interaction in the medium's interfaces. We also explore the existence of a response that cannot be reproduced if magnetic permeability variations are ignored.

2 Electromagnetic rock properties

For ground penetrating radar, the equations that govern the electromagnetic phenomenon are Maxwell's equations, which, in vector notation, are written as:

$$\nabla \cdot \mathbf{D} = \rho, \tag{1}$$

$$\nabla \cdot \mathbf{B} = 0, \tag{2}$$

$$\nabla \times \mathbf{E} = -\frac{\partial \mathbf{B}}{\partial t}, \tag{3}$$

and

$$\nabla \times \mathbf{H} = \mathbf{J} + \frac{\partial \mathbf{D}}{\partial t}. \tag{4}$$

In these expressions, $\mathbf{E}$ is the electric field vector, ρ is the electric charge density, $\mathbf{H}$ is the magnetic field vector, $\mathbf{J}$ is the electric current density vector, $\mathbf{B}$ is the magnetic flux density and $\mathbf{D}$ is the electric displacement. To fully couple these equations, we consider the constitutive relationships for linear, isotropic and non-dispersive materials given by: $\mathbf{D} = \varepsilon \mathbf{E}$, $\mathbf{B} = \mu \mathbf{H}$ and $\mathbf{J} = \sigma \mathbf{E}$.

More commonly, ε is expressed as a relative permittivity (ε_r- dimensionless) with respect to permittivity in the vacuum ($\varepsilon_o = 8.854 \times 10^{-12} F/m$) as $\varepsilon = \varepsilon_r \varepsilon_o$; similarly, the magnetic permeability can be expressed in terms of the permeability of free space (μ_o) as $\mu = \mu_r \mu_o$, where $\mu_o = 4\pi \times 10^{-7} H/m$ and μ_r is the relative permeability (dimensionless).

In a magnetically homogeneous medium, Equations 3,4, can be combined in a single expression, known as the Helmholtz equation for EM propagation:

$$\nabla^2 \mathbf{E} - \mu\varepsilon \frac{\partial^2 \mathbf{E}}{\partial t^2} - \mu\sigma \frac{\partial \mathbf{E}}{\partial t} = 0. \tag{5}$$

For a magnetically heterogeneous medium, however, the Helmholtz equation is more complex, and a different scheme is preferred for modeling (Noh et al., 2016; Pavlov and Zhdanov, 2001). Despite this, in electromagnetic modeling, it is common practice to assume either that variations in μ are small and to consider $\mu = \mu_0$ or to attribute all the differences in geophysical responses to ε or σ variations. In GPR applications, the most obvious choice is to combine these three properties into two coefficients ($\mu\varepsilon$ and $\mu\sigma$); however, as we may observe in the

FIGURE 5
Schematic FDTD algorithm flowchart for numerical modeling.
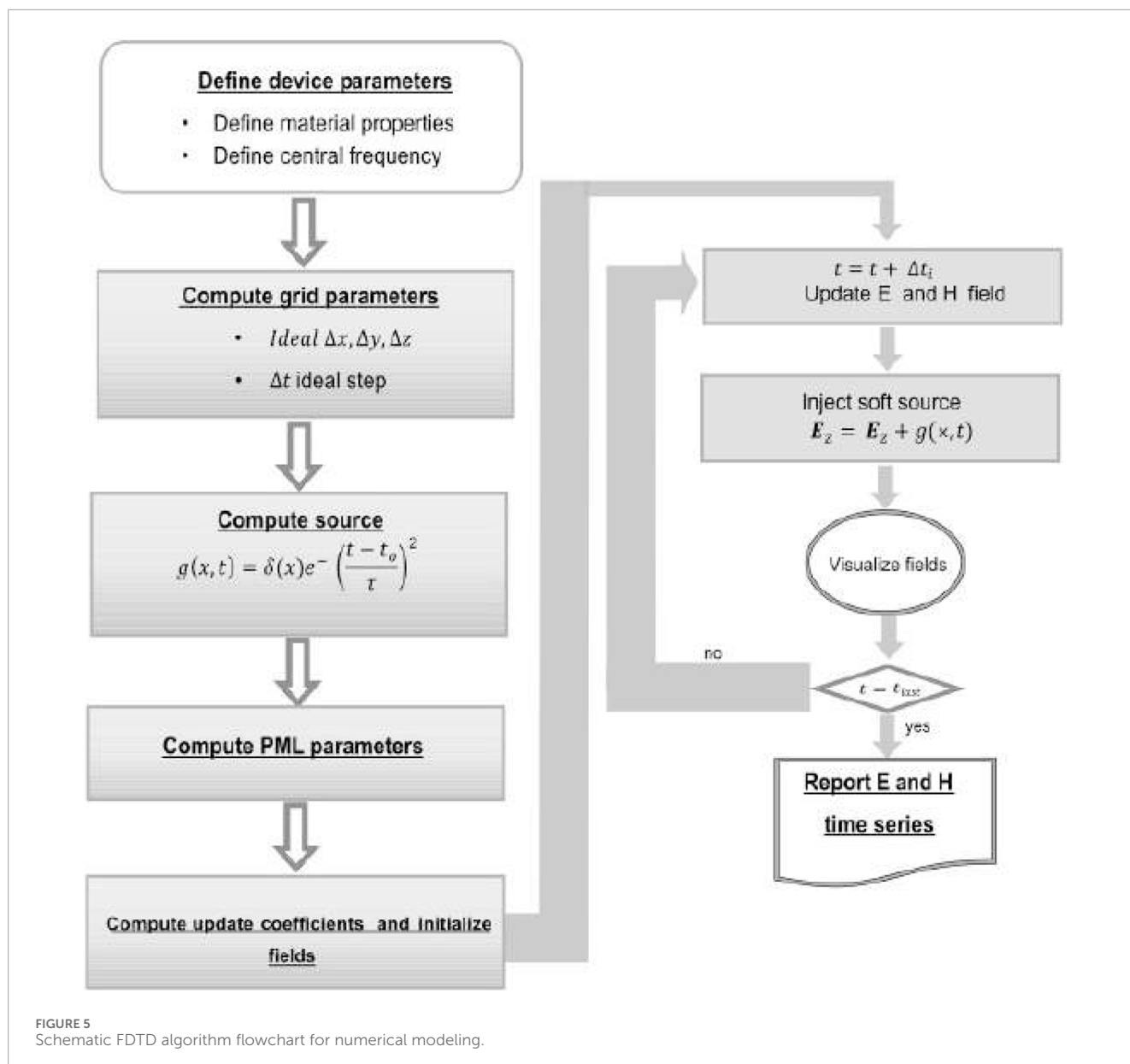
following sections, this assumption has noticeable consequences in the numerical modeling of electromagnetic fields in heterogeneous materials.
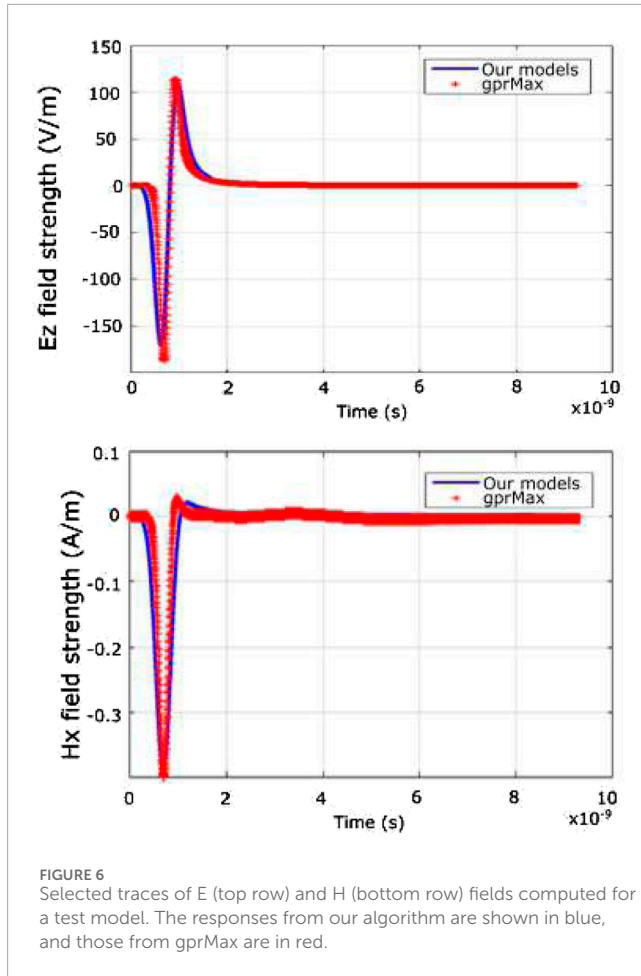
The importance of considering magnetic permeability in EM modeling starts from their natural variations in minerals and rocks. It is currently acknowledged that common Earth materials have at least a two-order of magnitude variation in each one of these three electromagnetic properties (Figures 1–3); therefore it seems reasonable that they all may produce an electromagnetic radar response. From the comparative analysis of the summarizing figures, we can remark the following:

1. The material's dielectric permittivity varies within a much narrower range than conductivity, even under the influence of various fluid (water or air) concentrations. Variations are due to particular sample conditions such as its porosity, the presence of water, its degree of compaction, etcetera.

2. Within their ranges of variation, the presence of water influences notably both the dielectric permittivity and conductivity, whereas magnetic permeability is particularly independent of the water content. In fact, magnetic permeability is the electromagnetic property most influenced directly by mineral composition.

3. Some common target materials in radar exploration, such as basalt, polar ice, etc., can be equivocally characterized by the combined values of the three properties.

Conceding that, for Earth materials, heterogeneities in the three EM properties exist and are relevant, we now face the challenge of computing their influence in radar data using directly Equations 1–4.

FIGURE 6
Selected traces of E (top row) and H (bottom row) fields computed for a test model. The responses from our algorithm are shown in blue, and those from gprMax are in red.

3 FDTD numerical modeling of radar signals for full heterogeneous models

Finite-difference time-domain (FDTD)

The FDTD method allows solving a coupled set of equations in discrete steps in time and space. It has long been used as a common strategy in seismological modeling, e.g., Virieux and Madariaga (1982), and Komatitsch and Martin (2007), among others. In electromagnetic modeling for geophysical applications, the method has been widely used since the early 90s (Holliger and Bergmann, 1998; Lampe et al., 2003; Cabrer et al., 2022); many of these publications, however, consider μ equal to μ_o.

We start our development from Equations 3, 4, using a leapfrog scheme to approximate the time derivatives. The time-step leapfrog scheme was first applied to the solution of Maxwell's equations by Yee (1966). The Yee cell discretizes the electric and magnetic fields in time and space so that both fields are intertwined. This scheme is known to be second-order accurate, enables computationally efficient time progress, and reduces memory storage.

For the three-dimensional case, Faraday's and Ampere's Equations 3, 4 can be expressed as follows:

$$\frac{\partial E_x}{\partial t} = \frac{1}{\varepsilon}\left(\frac{\partial H_z}{\partial y} - \frac{\partial H_y}{\partial z} - \sigma E_x - J_x \right), \qquad (6)$$

$$\frac{\partial E_y}{\partial t} = \frac{1}{\varepsilon}\left(\frac{\partial H_x}{\partial z} - \frac{\partial H_z}{\partial x} - \sigma E_y - J_y \right), \qquad (7)$$

$$\frac{\partial E_z}{\partial t} = \frac{1}{\varepsilon}\left(\frac{\partial H_y}{\partial x} - \frac{\partial H_x}{\partial y} - \sigma E_z - J_z \right), \qquad (8)$$

$$\mu\frac{\partial H_x}{\partial t} = -\left(\frac{\partial E_z}{\partial y} - \frac{\partial E_y}{\partial z} \right), \qquad (9)$$

$$\mu\frac{\partial H_y}{\partial t} = -\left(\frac{\partial E_x}{\partial z} - \frac{\partial E_z}{\partial x} \right), \qquad (10)$$

and

$$\mu\frac{\partial H_z}{\partial t} = -\left(\frac{\partial E_y}{\partial x} - \frac{\partial E_x}{\partial y} \right). \qquad (11)$$

We apply the FDTD scheme in a Yee (1966) grid to Equations 6–11. A schematic diagram of the Yee array is presented in Figure 4 and the relevant update equations for the E_x and H_x components are given by Equations 12, 13:

$$E_x|_{t+\Delta t}^{i,j,k} = \frac{\left(1 - \frac{\Delta t\sigma|^{i,j,k}}{2\varepsilon|^{i,j,k}}\right)}{\left(1 + \frac{\Delta t\sigma|^{i,j,k}}{2\varepsilon|^{i,j,k}}\right)} E_x|_t^{i,j,k} + \frac{1}{\left(1 + \frac{\Delta t\sigma|^{i,j,k}}{2\varepsilon|^{i,j,k}}\right)}\frac{\Delta t}{\varepsilon|^{i,j,k}\Delta y}\left(H_z|_{t+\Delta t/2}^{i,j,k} - H_z|_{t+\Delta t/2}^{i,j-1,k}\right)$$
$$- \frac{1}{\left(1 + \frac{\Delta t\sigma|^{i,j,k}}{2\varepsilon|^{i,j,k}}\right)}\frac{\Delta t}{\varepsilon|^{i,j,k}\Delta z}\left(H_y|_{t+\Delta t/2}^{i,j,k} - H_y|_{t+\Delta t/2}^{i,j,k-1}\right) \qquad (12)$$

and

$$H_x|_{t+\Delta t/2}^{i,j,k} = H_x|_{t-\Delta t/2}^{i,j,k} - \frac{\Delta t}{\mu|^{i,j,k}\Delta y}\left(E_z|_t^{i,j+1,k} - E_z|_t^{i,j,k}\right)$$
$$+ \frac{\Delta t}{\mu|^{i,j,k}\Delta z}\left(E_y|_t^{i,j,k+1} - E_y|_t^{i,j,k}\right). \qquad (13)$$

For a two-dimensional case, the EM fields propagate in two fully-decoupled modes: the transverse electric (TE) and the transverse magnetic (TM) modes.

We will work with the TM mode, where the update equations for E_z (Equation 14), H_x (Equation 15) and H_y (Equation 16) are:

$$E_z|_{t+\Delta t}^{i,j} = \frac{\left(1 - \frac{\Delta t\sigma|^{i,j}}{2\varepsilon|^{i,j}}\right)}{\left(1 + \frac{\Delta t\sigma|^{i,j}}{2\varepsilon|^{i,j}}\right)} E_z|_t^{i,j} + \frac{1}{\left(1 + \frac{\Delta t\sigma|^{i,j}}{2\varepsilon|^{i,j}}\right)}\frac{\Delta t}{\varepsilon|^{i,j}\Delta x}\left(H_y|_{t+\Delta t/2}^{i,j} - H_y|_{t+\Delta t/2}^{i-1,j}\right)$$
$$- \frac{1}{\left(1 + \frac{\Delta t\sigma|^{i,j}}{2\varepsilon|^{i,j}}\right)}\frac{\Delta t}{\varepsilon|^{i,j}\Delta y}\left(H_x|_{t+\Delta t/2}^{i,j} - H_x|_{t+\Delta t/2}^{i,j-1}\right) \qquad (14)$$

for the electric z component, and:

$$H_x|_{t+\Delta t/2}^{i,j} = H_x|_{t-\Delta t/2}^{i,j} - \frac{\Delta t}{\mu|^{i,j}\Delta y}\left(E_z|_t^{i,j+1} - E_z|_t^{i,j}\right) \qquad (15)$$

and

$$H_y|_{t+\Delta t/2}^{i,j} = H_y|_{t-\Delta t/2}^{i,j} + \frac{\Delta t}{\mu|^{i,j}\Delta x}\left(E_z|_t^{i+1,j} - E_z|_t^{i,j}\right) \qquad (16)$$

for the magnetic x and y components.

Similarly, for the one-dimensional FDTD case, the Maxwell's equations are reduced to:

$$E_x|_{t+\Delta t}^{k} = \frac{\left(1 - \frac{\Delta t\sigma|^{k}}{2\varepsilon|^{k}}\right)}{\left(1 + \frac{\Delta t\sigma|^{k}}{2\varepsilon|^{k}}\right)} E_x|_t^{k} - \frac{1}{\left(1 + \frac{\Delta t\sigma|^{k}}{2\varepsilon|^{k}}\right)}\frac{\Delta t}{\varepsilon|^{k}\Delta z}\left(H_y|_{t+\Delta t/2}^{k} - H_y|_{t+\Delta t/2}^{k-1}\right)$$
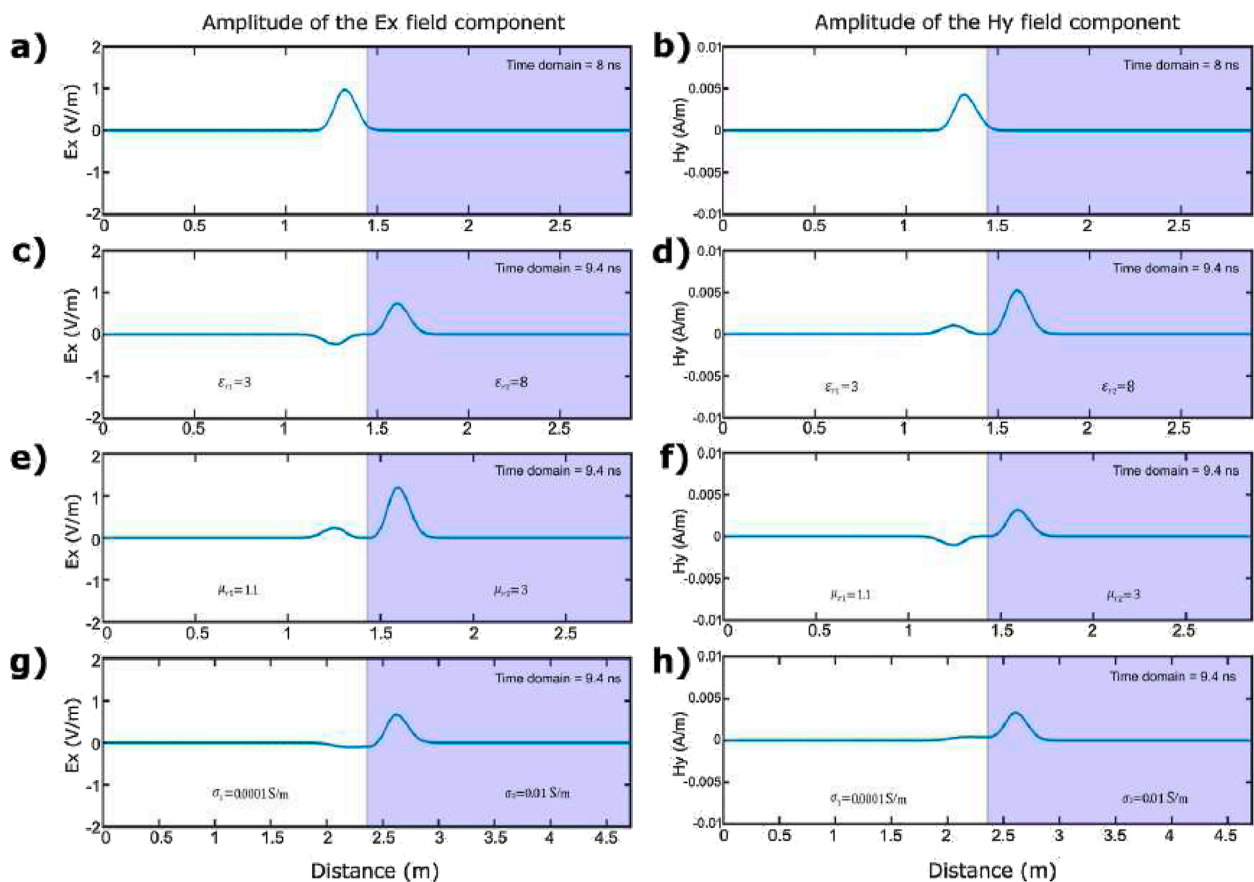$$\qquad (17)$$

FIGURE 7
Electric (left) and magnetic (right) fields for two contrasting layers, considering separated variations for ε_r, μ_r and σ. The **(a)** and **(b)** panels represent the EM wave before it arrives at the transition zone. The **(c)** and **(d)** correspond with variations only in ε. In **(e)** and **(f)** traces, the propagation corresponds with $\mu_{r1} = 1.1$ for the first medium and $\mu_{r2} = 3$ for the second in blue. Finally, only the electrical conductivity σ is changing in the **(g)** and **(h)** panels. Notice the differences in the amplitude and polarity of the transmitted and reflected waves in the transition zone in each one of the cases.

and

$$H_y\big|_{t+\Delta t/2}^{k} = H_y\big|_{t-\Delta t/2}^{k} - \frac{\mu\big|^{k}\Delta t}{\Delta z}\left(E_x\big|_t^{k+1} - E_x\big|_t^{k}\right). \quad (18)$$

The above equations represent the necessary components for the 1D and 2D electromagnetic wave propagation for numerical modeling.

In all our experiments, an incoming Gaussian signal with central frequency 200 MHz was used as a source. To have an adequate discrete representation the grid spacing must be sufficiently small to resolve the shortest wavelength. For this, we select 35 point per wave length ($_{min}(\Delta x, \Delta y, \Delta z) \leq v/35f$, where v is the speed of propagation of the wave and f the frequency), that is superior to the Nyquist sample criterion. To ensure numerical stability, the time-space steps are constrained to satisfy the Courant-Friedrich-Lewy (CFL) condition:

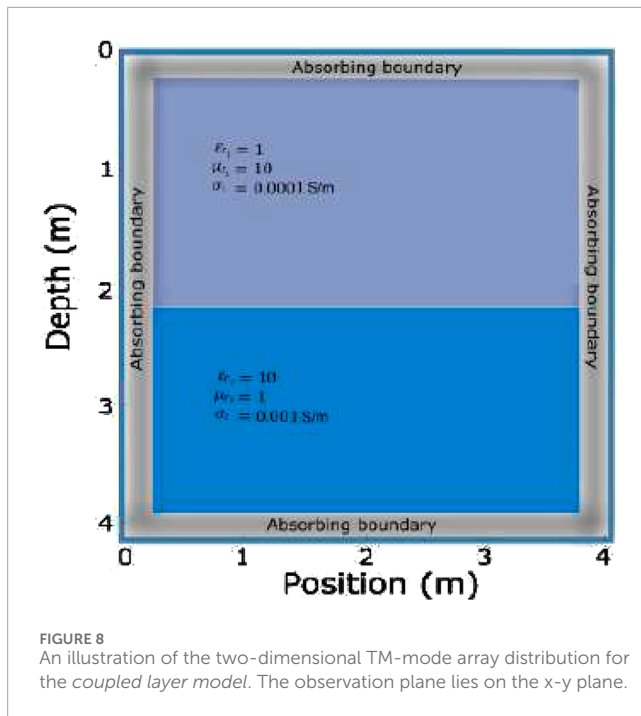$$\Delta t < \frac{1}{c_o\sqrt{\frac{1}{\Delta x^2} + \frac{1}{\Delta y^2} + \frac{1}{\Delta z^2}}}. \quad (19)$$

To reduce spurious waves reflected from the edges of the model we adapt the Perfectly Matched Layer (PML) method for the coupled solution of Ampere's and Faraday's laws considering the three EM properties, (e.g., Berenger, 1994). The basic considerations for developing this formulation can be found in Supplementary Appendix A. The adapted PML equations for the corresponding Equations 14, 15, for the two-dimensional TM mode:

$$E_z\big|_{t+\Delta t}^{i,j} = m_{Ez1}E_z\big|_t^{i,j} + \frac{1}{d_{Ez}}\left(\frac{\Delta t}{\varepsilon|^{i,j}}C_z^{H}\big|_{t+\Delta t/2}^{i,j}\right) + \frac{1}{d_{Ez}}\left(-\frac{\sigma_x'|^{i,j}\sigma_y'|^{i,j}\Delta t^2}{\varepsilon|^{i,j}\varepsilon_o^2}IE_z\big|_t^{i,j}\right), \quad (20)$$

where σ_x' and σ_y' are the fictitious values for the PML formulation, and:

$$d_{Ez} = 1 + \frac{\sigma_x'|^{i,j} + \sigma_y'|^{i,j}\Delta t}{2\varepsilon_o} + \frac{\sigma_x'|^{i,j}\sigma_y'|^{i,j}\Delta t^2}{4\varepsilon_o^2} + \frac{\sigma|^{i,j}\Delta t}{2\varepsilon|^{i,j}}, \quad (21)$$

$$m_{Ez1} = \frac{\left(1 - \frac{\sigma_x'|^{i,j}+\sigma_y'|^{i,j}\Delta t}{2\varepsilon_o} - \frac{\sigma_x'|^{i,j}\sigma_y'|^{i,j}\Delta t^2}{4\varepsilon_o^2} - \frac{\sigma|^{i,j}\Delta t}{2\varepsilon|^{i,j}}\right)}{d_{Ez}}, \quad (22)$$

FIGURE 8
An illustration of the two-dimensional TM-mode array distribution for the *coupled layer model*. The observation plane lies on the x-y plane.

$$IE_z|_t^{i,j} = \sum_{t=0}^{T} E_z|_t^{i,j}; \quad C_z^H|_{t+\Delta t/2}^{i,j} = \frac{H_y|_{t+\Delta t/2}^{i,j} - H_y|_{t+\Delta t/2}^{i-1,j}}{\Delta x} - \frac{H_x|_{t+\Delta t/2}^{i,j} - H_x|_{t+\Delta t/2}^{i,j-1}}{\Delta y}. \tag{23}$$

Similarly, the *Hx* component is giving by:

$$H_x|_{t+\Delta t/2}^{i,j} = m_{Hx1} H_x|_{t-\Delta t/2}^{i,j} + \frac{1}{d_{Hx}}\left(-\frac{\Delta t}{\mu|^{i,j}} C_x^E|_t^{i,j}\right) + \frac{1}{d_{Hx}}\left(-\frac{\sigma'_x|^{i,j}\Delta t^2}{\varepsilon_o \mu} I_{CEx}|_t^{i,j}\right), \tag{24}$$

with the coefficients:

$$d_{Hx} = 1 + \frac{\sigma'_y|^{i,j}\Delta t}{2\varepsilon_o}; \quad m_{Hx1} = \frac{\left(1 - \frac{\sigma'_y|^{i,j}\Delta t}{2\varepsilon_o}\right)}{d_{Hx}}; \quad I_{CEx}|_t^{i,j} = \sum_{t=0}^{T} C_x^E|_t^{i,j}; \tag{25}$$

$$C_x^E|_t^{i,k} = \frac{E_z|_t^{i,j+1} - E_z|_t^{i,j}}{\Delta y}. \tag{26}$$

The Equations 12, 13, which correspond to the 3D formulation, were developed for future work; however, in the following sections, we focus our results on one and two-dimensional models. In this context, the Equations 16–26 were used for modeling the EM propagation. The implemented flowchart of the algorithms is shown in Figure 5.

As a first test to gauge the results obtained from this algorithm, we compare the fields computed for a homogeneous medium with those of the well-known software *gprMax* (Warren et al., 2016). For this experiment we set $\varepsilon_r = 3$, $\mu_r = \mu_0$ and $\sigma = 0.00001$ S/m and selected a source with a central frequency of 300 MHz. In Figure 6 we superimpose the *Ez* and *Hx* field components traces from our FDTD algorithm and those resulting from gprMax. As seen in the traces, the waveforms resemble each other within one order of magnitude and may be considered a fair approximation for the numerical modeling.

4 The magnetic permeability in the transmission and reflection of em waves

In the following numerical experiments, we consider variations in each EM property to analyse the influence of each one of them on the radar signal and its combination for a simultaneous effect. We modelled electric and magnetic components to analyse the effect in both fields.

Since EM field propagation depends on dielectric permittivity, electrical conductivity and magnetic permeability, we expect that each one of these properties affects the radar signal differently, and even though their effects combine into a single EM signal, they can still be individually distinguished. So, to identify their combined effects, we resource to one and two-dimensional models with different physical properties and compute the electric and magnetic fields as they propagate through the media.

To illustrate and explain the differences in reflectivity mechanisms when facing electromagnetic ε, μ or σ property contrast we use a model with two contacting homogeneous media (Figure 7). The top panels show fields at time 8 ns when they are still travelling through the first media with εr1=3, μr1=1.1and σ1=0.0001 S/m". In the following rows, we illustrated the same fields at time 9.4 ns once the signal impinged on the contrasting interface varying only permittivity (εr2=8, Figures 7c, d), magnetic permeability (μr2=3, Figures 7e, f) and conductivity (σ2=0.01 S/m, Figures 7g, h)." From our results, we may summarize the following observations: a) a change in properties determines the fraction of energy transmitted or reflected in both media, b) the polarity of the reflected with respect to the transmitted wave changes in E and H fields, this change in polarity provides evidence whether the change is in ε or μ and c) conductivity produces mainly an attenuation effect in the signal.

From these 1D experiments, however, we cannot observe any implications related to geometrical divergence. For this, we conducted the two-dimensional experiments of the following sections. In the example from the next section, we explore a 2D EM wave propagation through two media with identical wave speed and attenuation constants, but different μ values so as to make both layers equivalent in the Helmholtz framework. We refer to this example as the *coupled-layer model*, which is intended to prove the need to include the magnetic permeability in high-frequency EM modeling, and the detectability of two layers for their sole change in μ. In the last example, the effect of the magnetic permeability contrast on the GPR signal is tested on an archaeologically relevant target.

4.1 Testing the need of magnetic permeability in a "coupled-layer model"

Although the theoretical EM framework makes it obvious that signal depends on μ, posing an example where its effect is isolated from the other two properties does not exist in the publish literature. For this, we design a *coupled layer model* with two media with different EM properties but identical wave speed ($\varepsilon\mu$) and attenuation ($\sigma\mu$) factors (Figure 8). In this experiment, an incoming Gaussian signal with a central frequency of 200 MHz was
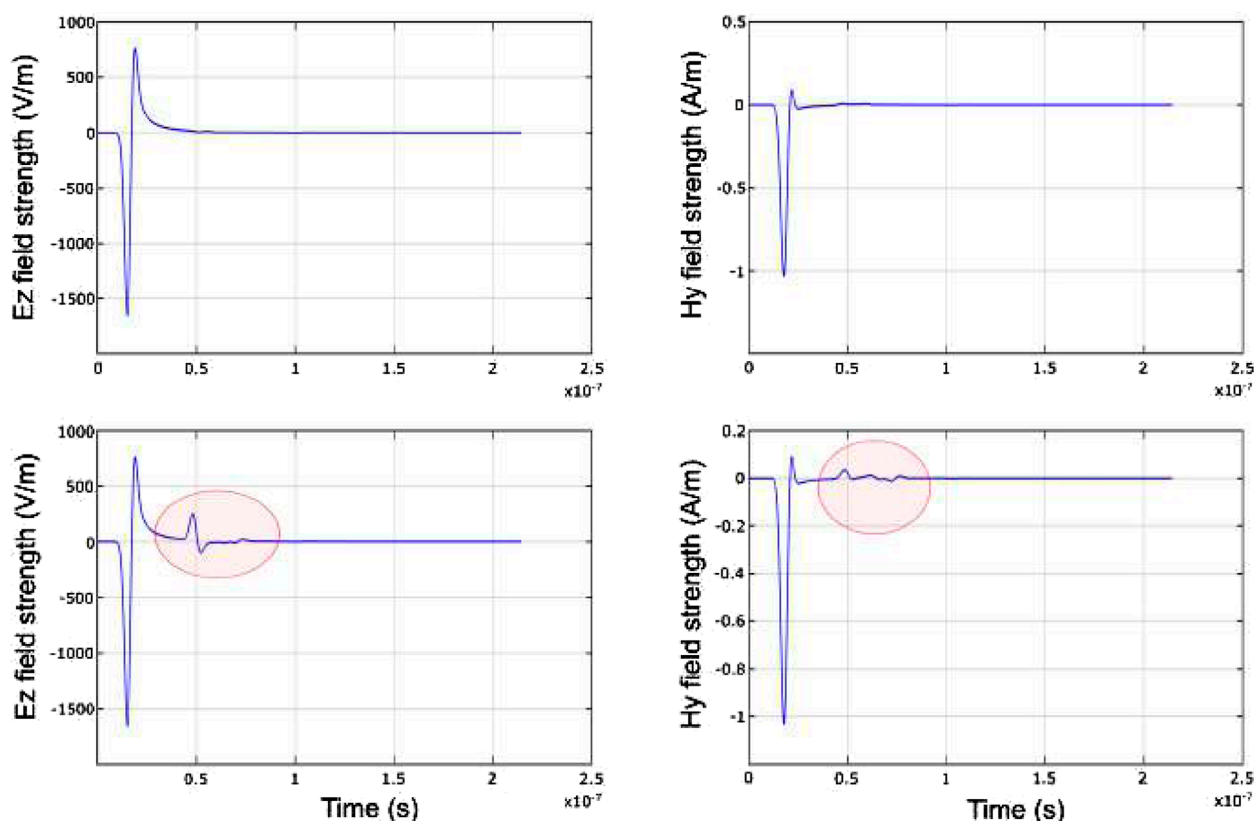
FIGURE 9
E (left) and H (right) field traces for a model that includes variations in the three properties, designed for the *coupled layer model* ($\varepsilon_{r_1}\mu_{r_1} = \varepsilon_{r_2}\mu_{r_2}$, and $\sigma_1\mu_{r_1} = \sigma_2\mu_{r_2}$). The traces in the top panels show a propagation when $\mu_{r_1} = \mu_{r_2} = \mu_0$. Bottom panels show traces when $\mu_{r_1} \neq \mu_{r_2}$. Circles mark the reflected wave unpredicted by the conventional radar modeling.

sampled with 35 points per wavelength to have an adequate discrete representation.

Following Figure 8, we set $\varepsilon_{r_1} = 1$, $\mu_{r_1} = 10$ and $\sigma_1 = 0.0001$ S/m for the upper layer and $\varepsilon_{r_2} = 10$, $\mu_{r_2} = 1$ and $\sigma_2 = 0.001$ S/m for the deepest layer. In this model, $\varepsilon\mu$ and $\sigma\mu$ products are the same for both media, so, according to the Helmholtz framework, the propagation of the electromagnetic wave through all numerical space should be identical.

Figure 9 shows the electric and magnetic field traces at an observation point at the surface. In the first row of Figure 9, the magnetic permeability is set equal to μ_o (as it is commonly assumed in radar modeling so $\mu_{r1} = \mu_{r2} = \mu_o$). The second row of Figure 9, shows the field for the coupled layer model considering layers with equivalent wavelength, velocity, attenuation, and discretization parameters but $\mu \neq \mu_o$. In these traces, the reflected wave at time $0.5 \times 10^{-7} s$ (marked with a red circle) can only be predicted if magnetic permeability contrasts are considered for numerical modeling.

The snapshots and shot gathers in Figure 10 show the actual EM wave travelling through the same coupled layer model. Note that the marked reflection would not exist if magnetic permeability was constant, as in the Helmholtz framework (Equation 5). While this example may be difficult to find in nature, it should make evident the need to include magnetic contrast in the numerical modeling of high frequency EM waves, otherwise, the wave propagation would act as

if there were only one propagation medium and the signal masks the transition zone.

These experiments show the need to consider magnetically heterogeneous media, which is not implemented in most geophysical EM modeling approaches.

4.2 Testing the relevance of magnetic permeability: the Olmec head example

The Olmec heads (Figure 11) are sculptures of members of the nobility of the ancient Olmec culture carved in volcanic stone. These sculptures were found in Quaternary coastal alluvial deposits associated with the currents of the Coatzacoalcos and Uxpana rivers in San Lorenzo Veracruz, Mexico. These $1 - 2.7$ m sized stone boulders are allochthonous to the river bank and were brought from the Cerro Cintepec volcano near the Sierra of Los Tuxtlas. As many as 124 stone sculptures have been discovered since the 60s and some geophysical studies were developed in the area, starting from the pioneering work of Breiner and Coe (1972), and it is suspected more are still buried.

Despite their size and allochthonous origin, precise identification of these colossal archaeological remains may still be an interesting target for GPR surveys. Besides natural water moisture
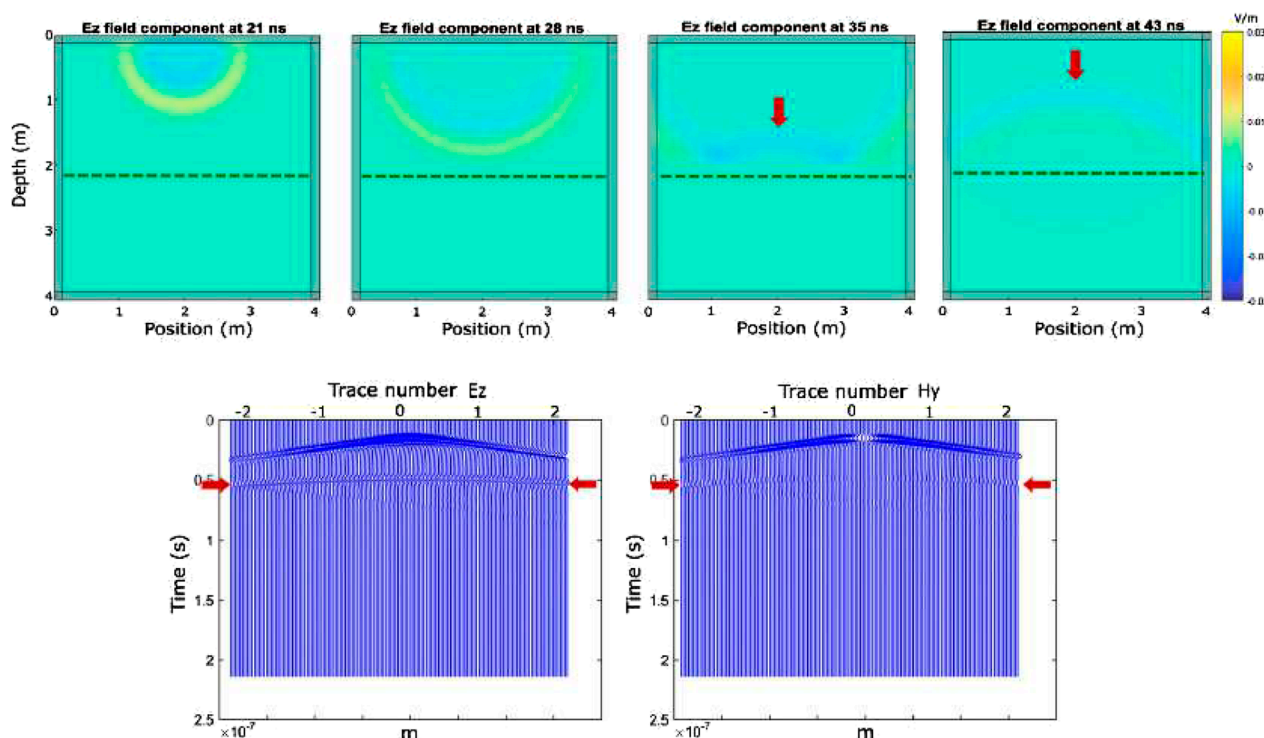
FIGURE 10
Two-dimensional snapshots (top panels) and radar trace gathers (bottom panels) for the EM wave propagated through the model illustrated in Figure 8. The dotted line in each snapshot indicates the location of the layer boundary; the reflection remarked with red arrows cannot be recovered if μ is considered as μ_o.
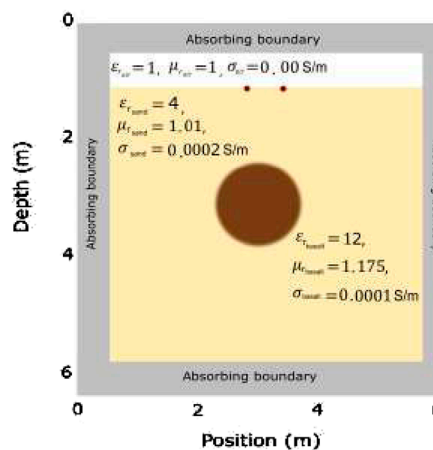

FIGURE 11
Historic photograph and schematic diagram of the Olmec Head example (left) and our selected model parameters for the Olmec example (right). Image credit Richard Hewitt Stewart/National Geographic Creative, Olmec Colossal Head, Monument 1, San Lorenzo, 1946, in Matthew Stirling, National Geographic, Washington.

alterations, the magnetic permeability of the basalt stone may be the most contrasting feature, and its identification in the signal should lead to the distinction of these volcanic boulders. In this scenario, modeling and identifying the magnetic permeability signal in the GPR data becomes a key element. In Figure 11, we sketch the hypothetical head models and our selected electromagnetic properties.

To illustrate the differences in the actual electric field propagating through the Olmec head, we present some snapshots in Figure 12. Note that after 18 ns, the wave reaches and interacts with the target.

To simulate the GPR response of these archaeological remains, we used characteristic properties of the material where the Olmec heads were discovered. The sedimentary rocks of the San Lorenzo
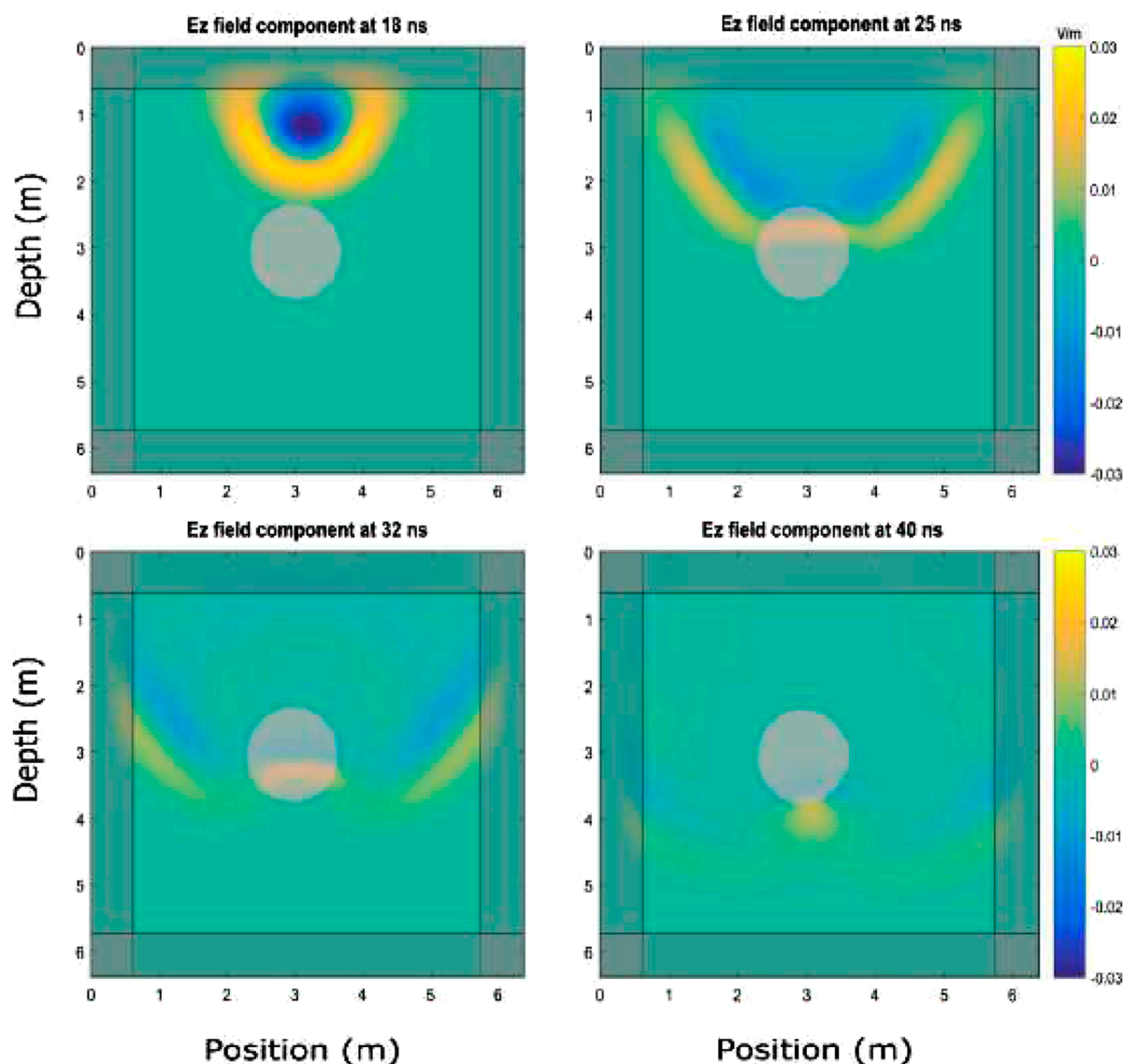
FIGURE 12
Selected 2D- *Ez* snapshots for the Olmec Head example. Circle denotes the location of the set basalt Olmec's Head, from the geometry models in Figure 11.

area correspond to Miocene and Jurassic deposits of coastal marine origin; they are a sequence of sands and clay sedimented in a marine and shallow-water environment. The rock materials in this area are structured in a layer of compacted coarse-grained sands with clays over finer-grained sands mixed with interspersed clays with high carbon content deposits. The basalt properties selected for the numerical models of Figure 13 are different for μ_r, but ε_r and σ are held constant for all the examples ($\varepsilon_{r_{basalt}} = 12$ and $\sigma_{basalt} = 0.0001$ S/m).

Figure 13 shows an example of our computed *E*- and *H*- fields. For this experiment, we explore three scenarios using the magnetic permeability values for basalt from the seminal work of Breiner and Coe (1972) in the area of San Lorenzo: i) $\mu_{r_{basalt}} = 1$ (the standard assumption), ii) $\mu_{r_{basalt}} = 2.5$ and iii) $\mu_{r_{basalt}} = 4.5$. In this example, the

hypothetical Olmec head is approximately 1 m in size and is buried at 0.6 m.

We can notice interesting differences in the waveform, amplitude and travel time of the reflected EM wave on the set target. These differences result solely from magnetic permeability variations, confirming the relevance of μ for this archaeological target.

In Figure 13, we observe that the first reflected wave increases its amplitude when μ increases (red dot line), whereas the second reflected wave (marked with a red circle) delays and decreases its amplitude when traversing through the Olmec head with an increased magnetic property. Additionally, we can notice an attenuation of the second reflected wave with the increment in magnetic permeability, so we can conclude that magnetic properties have a characteristic combined effect on the amplitude and delay of the radar signal.
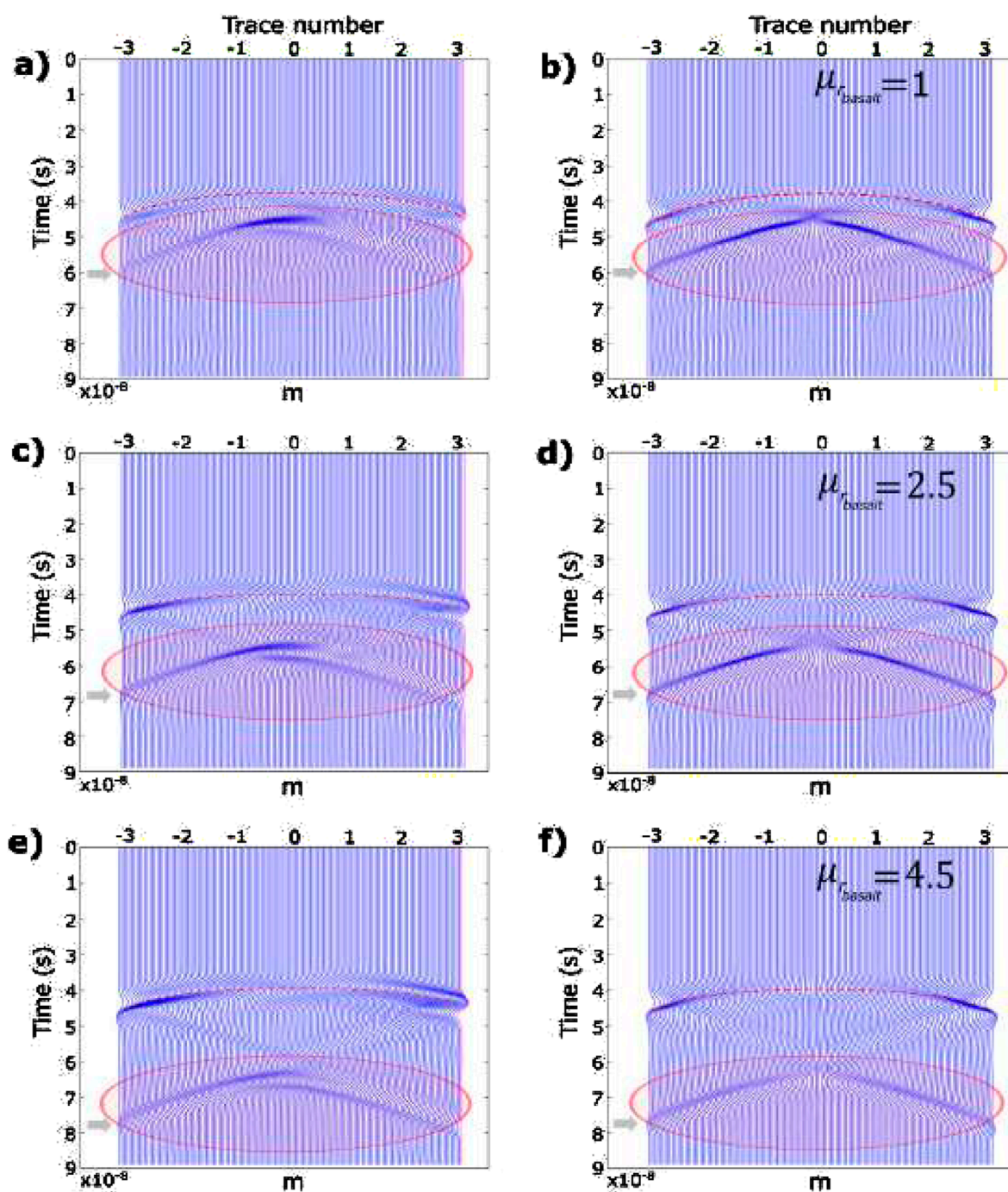
FIGURE 13
Two-dimensional radargrams for the *Ez* (left) and *Hy* (right) components for the Olmec Head example. The **(a,b)** panels correspond with $\mu_{r_{basalt}} = 1$ as in a traditional radar scheme modeling. Notice the effect from **(c–f)** panels because of the increment in magnetic permeability, highlighted with red circles. If the variations in magnetic permeability are not considered for modeling, these effects go unnoticed.

To simulate a more realistic scenario for the San Lorenzo examples and explore the complexity added by a conductive layer, we added a hypothetical clay layer above and below the Olmec head. The results (Figure 14) show that the clay layer attenuates the EM signal effectively (see the red blur mark and arrows in the figure); however, the position and thickness of this clay layer may either mask (top panels) or enhance (bottom panels) the target radar response. This effect is especially noticeable for the magnetic field component (right columns).

In general, we observed that the magnetic permeability contrast notably influences the GPR response, thus facilitating the detection of the target and setting the path for the joint inversion of magnetic and GPR data for any modern archaeological exploration.
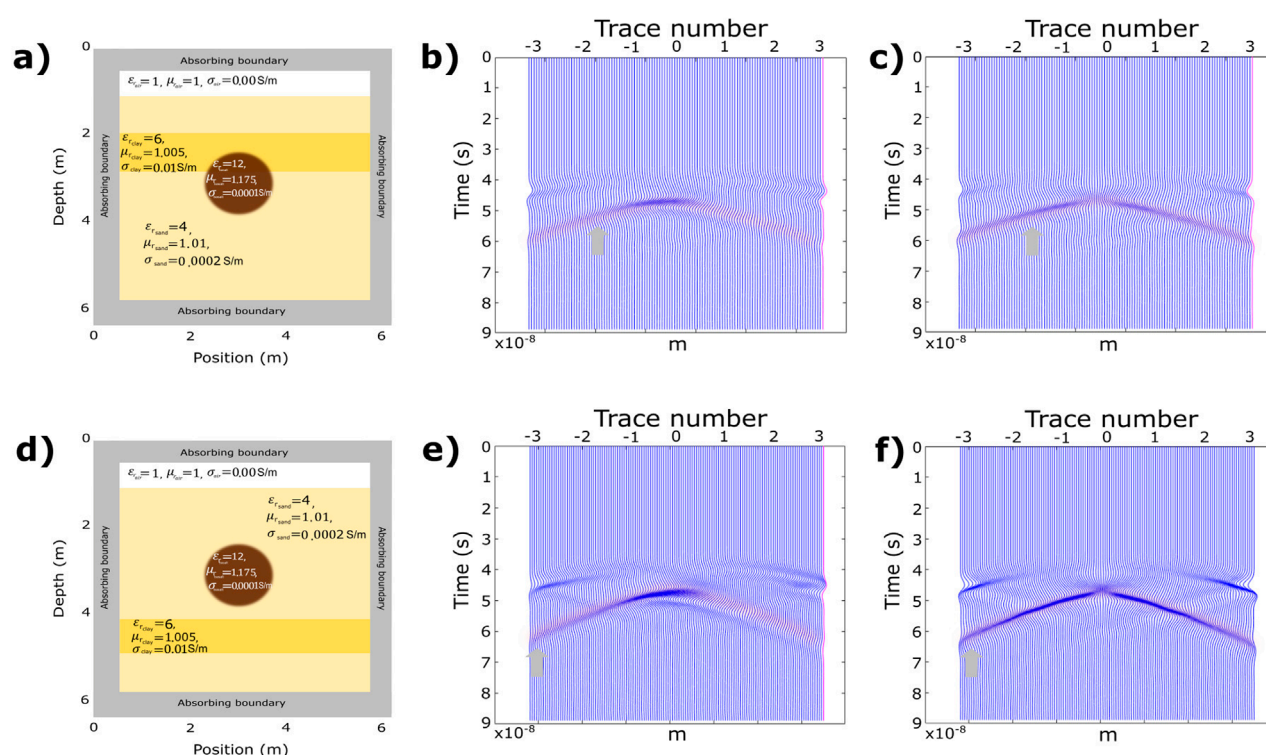
FIGURE 14
Two-dimensional radargrams for the *Ez* (left) and *Hy* (right) components for the Olmec Head example, including a clay cap. The **(a,d)** panels correspond to the diagrams showing the clay cap position (thin yellow layer). The b, c, e and f panels correspond to the radargrams for the electric **(b,e)** and magnetic **(c,f)** components.

5 Conclusion

In this work, a staggered E-H FDTD algorithm for radar modeling was developed by using a coupled Faraday-Ampere framework. The method considers heterogeneities in the three EM properties for radar signal modeling: dielectric permittivity, magnetic permeability and electrical conductivity.

As expected, when the EM wave travels through an homogeneous media, each property affects their transit differently: permittivity determines the wave propagation velocity and electrical conductivity the wave attenuation whereas magnetic permeability influences both aspects. Notably, our results show that the polarity of the reflected vs. transmitted waves are very insightful; a change in ε reverses the polarity of the E field and μ reverses the polarity of the H field.

Contrasting values in the magnetic permeability affect not only the transmission/diffusion of the EM wave but also the interactions in the interfaces, resulting in reflected and transmitted waves that cannot be replicated with the sole combination of ε and σ.

Our experiments show how measuring E and H fields allows distinguishing variations from the three properties. Currently, magnetic field components are not considered in radar despite the fact they may contribute to the GPR signal interpretation.

Whereas the combined effect of the radar properties in the GPR signal can make their interpretation challenging, the possibility of use a full three electromagnetic property and both E-H fields

propagation for numerical modeling algorithms should lead to a more accurate and discriminative interpretation of the data. Concurrently, the potential acquisition of magnetic field in radar surveys may also contribute to a more unique characterization of the causing heterogeneities.

Given all these possibilities, it is interesting to consider magnetic permeability not only in archaeological examples but also in other applications where magnetic properties may be prominent, such as unexploded ordnances, extraterrestrial explorations, borehole studies and geotechnical studies.

Data availability statement

The data supporting the findings of this study will be made available by the authors upon justified request.

Author contributions

AS: Conceptualization, Formal Analysis, Investigation, Methodology, Software, Visualization, Writing – original draft, Writing – review and editing. LG: Conceptualization, Formal Analysis, Supervision, Validation, Writing – review and editing, Funding acquisition, Methodology.

Funding

Acknowledgments

Conflict of interest

The authors declare that the research was conducted in the absence of any commercial or financial relationships that could be construed as a potential conflict of interest.

Generative AI statement

The author(s) declare that no Generative AI was used in the creation of this manuscript.

Publisher's note

All claims expressed in this article are solely those of the authors and do not necessarily represent those of their affiliated organizations, or those of the publisher, the editors and the reviewers. Any product that may be evaluated in this article, or claim that may be made by its manufacturer, is not guaranteed or endorsed by the publisher.

Supplementary material

The Supplementary Material for this article can be found online at: https://www.frontiersin.org/articles/10.3389/feart.2025.1632441/full#supplementary-material

References

Aditama, I. F., Syaifullah, K. I., and Saputera, D. H. (2015). "Detecting buried human bodies in graveyard with ground-penetrating radar," in *International workshop and gravity, electrical and magnetic methods and their applications* (China: Chenghu), 420–423. doi:10.1190/gem2015-109

Alonso-Díaz, A., Casado-Rabasco, J., Solla, M., and Lagüela, S. (2023). Using InSAR and GPR techniques to detect subsidence: application to the coastal area of "A Xunqueira" (NW Spain). *Remote Sens.* 15, 3729. doi:10.3390/rs15153729

Berenger, J.-P. (1994). A perfectly matched layer for the absorption of electromagnetic waves. *J. Comput. Phys.* 114, 185–200. doi:10.1006/jcph.1994.1159

Berezowski, V., Mallett, X., Simyrdanis, K., Kowlessar, J., Bailey, M., and Moffat, I. (2024). Ground penetrating radar and electrical resistivity tomography surveys with a subsequent intrusive investigation in search for the missing Beaumont children in Adelaide, South Australia. *Forensic Sci. Int.* 357, 111996. doi:10.1016/j.forsciint.2024.111996

Bianco, L., La Manna, M., Russo, V., and Fedi, M. (2024). Magnetic and GPR Data Modelling via Multiscale Methods in San Pietro in Crapolla Abbey, Massa Lubrense (Naples). *Archaeol. Prospect.* 31, 139–147. doi:10.1002/arp.1936

Breiner, S., and Coe, M. (1972). Magnetic exploration of the olmec civilization: magnetic surveys have been highly successful in locating olmec monuments at the site of the oldest known civilization in mesoamerica. *Am. Sci.* 60(5), 566–575.

Butler, D. K. (2012). What is near-surface geophysics? 1–6. doi:10.1190/1.9781560801719.ch1

Cabrer, R., Gallardo, L. A., and Flores, C. (2022). Implicit finite-difference time-domain schemes for TDEM modeling in three dimensions. *Geophysics* 87, E347–E358. doi:10.1190/geo2021-0587.1

Cassidy, N., Eddies, R., and Dods, S. (2011). Void detection beneath reinforced concrete sections: the practical application of ground-penetrating radar and ultrasonic techniques. *J. Appl. Geophys.* 74, 263–276. doi:10.1016/j.jappgeo.2011.06.003

Cassidy, N. J. (2008). Frequency-dependent attenuation and velocity characteristics of nano-to-micro scale, lossy, magnetite-rich materials. *Near Surf. Geophys.* 6, 341–354. doi:10.3997/1873-0604.2008023

Conyers, L. B., St Pierre, E. J., Sutton, M.-J., and Walker, C. (2019). Integration of GPR and magnetics to study the interior features and history of Earth mounds, Mapoon, Queensland, Australia. *Archaeol. Prospect.* 26, 3–12. doi:10.1002/arp.1710

Giannakis, I., Giannopoulos, A., and Warren, C. (2016). A realistic FDTD numerical modeling framework of ground penetrating radar for landmine detection. *IEEE J. Sel. Top. Appl. Earth Observations Remote Sens.* 9, 37–51. doi:10.1109/JSTARS.2015.2468597

Giannopoulos, A. (2005). Modelling ground-penetrating radar by GprMax. *Constr. Build. Mater.* 19, 755–762. doi:10.1016/j.conbuildmat.2005.06.007

Hamran, S.-E., Erlingsson, B., Gjessing, Y., and Mo, P. (1998). Estimate of the subglacier dielectric constant of an ice shelf using a ground-penetrating step-frequency radar. *IEEE Trans. geoscience remote Sens.* 36, 518–525. doi:10.1109/36.662734

Heagy, L. J., and Oldenburg, D. W. (2023). Impacts of magnetic permeability on electromagnetic data collected in settings with steel-cased Wells. *Geophys. J. Int.* 234, 1092–1110. doi:10.1093/gji/ggad122

Holliger, K., and Bergmann, T. (1998). Accurate and efficient FDTD modeling of ground-penetrating radar antenna radiation. *Geophys. Res. Lett.* 25, 3883–3886. doi:10.1029/1998GL900049

Klotzsche, A., Jonard, F., Looms, M. C., van der Kruk, J., and Huisman, J. A. (2018). Measuring soil water content with ground penetrating radar: a decade of progress. *Vadose Zone J.* 17, 1–9. doi:10.2136/vzj2018.03.0052

Komatitsch, D., and Martin, R. (2007). An unsplit convolutional perfectly matched layer improved at grazing incidence for the seismic wave equation. *Geophysics* 72, SM155–SM167. doi:10.1190/1.2757586

La Bruna, V., Araújo, R., Lopes, J., Silva, L., Medeiros, W., Balsamo, F., et al. (2024). Ground penetrating radar -based investigation of fracture stratigraphy and structural characterization in karstified carbonate rocks, Brazil. *J. Struct. Geol.* 188, 1. doi:10.1016/j.jsg.2024.105263

Lampe, B., Holliger, K., and Green, A. G. (2003). A finite-difference time-domain simulation tool for ground-penetrating radar antennas. *Geophysics* 68, 971–987. doi:10.1190/1.1581069

Lazaro-Mancilla, O., and Gómez-Treviño, E. (2000). Ground penetrating radar inversion in 1-D: an approach for the estimation of electrical conductivity, dielectric permittivity and magnetic permeability. *J. Appl. Geophys.* 43, 199–213. doi:10.1016/S0926-9851(99)00059-2

Molina, C. M., Wisniewski, K. D., Salamanca, A., Saumett, M., Rojas, C., Gómez, H., et al. (2024). Monitoring of simulated clandestine graves of victims using UAVs, GPR, electrical tomography and conductivity over 4-8 years post-burial to aid forensic search investigators in Colombia, South America. *Forensic Sci. Int.* 355, 111919. doi:10.1016/j.forsciint.2023.111919

Noh, K., Oh, S., Seol, S., Lee, K., and Byun, J. (2016). Analysis of anomalous electrical conductivity and magnetic permeability effects using a frequency domain controlled-source electromagnetic method. *Geophys. J. Int.* 204, 1550–1564. doi:10.1093/gji/ggv537

Olhoeft, G. (1998). "Electrical, magnetic, and geometric properties that determine ground penetrating radar performance," in *Proceedings of the SeventhInternational conference on ground penetrating radar*, 177–182.

Ortega-Ramírez, J., Bano, M., Cordero-Arce, M. T., Villa-Alvarado, L. A., and Fraga, C. C. (2020). Application of non-invasive geophysical methods (GPR and ERT) to locate the ancient foundations of the first cathedral of Puebla, Mexico. A case study. *J. Appl. Geophys.* 174, 103958. doi:10.1016/j.jappgeo.2020.103958

Palacky, G. J. (2012). Resistivity characteristics of geologic targets. 52–129. doi:10.1190/1.9781560802631.ch3

Pavlov, D. A., and Zhdanov, M. S. (2001). Analysis and interpretation of anomalous conductivity and magnetic permeability effects in time domain electromagnetic data: part I: numerical modeling. *J. Appl. Geophys.* 46, 217–233. doi:10.1016/S0926-9851(01)00040-4

Persico, R., Negri, S., Soldovieri, F., and Pettinelli, E. (2012). Pseudo 3D imaging of dielectric and magnetic anomalies from GPR data. *Int. J. Geophys.* 2012, 1–5. doi:10.1155/2012/512789

Pettinelli, E., Burghignoli, P., Pisani, A. R., Ticconi, F., Galli, A., Vannaroni, G., et al. (2007). Electromagnetic propagation of GPR signals in Martian subsurface scenarios including material losses and scattering. *IEEE Trans. Geoscience Remote Sens.* 45, 1271–1281. doi:10.1109/tgrs.2007.893563

Qiao, S., Zhong, P., Zheng, X., Yi, M., Shu, T., Wang, Q., et al. (2025). Three-dimensional marine magnetotelluric modeling in anisotropic media using finite-element method with coupled perfectly matched layer boundary conditions. *J. Phys. Conf. Ser.* 3007, 012048. doi:10.1088/1742-6596/3007/1/012048

Reichard, J. (2020). *Environmental geology*. McGraw-Hill Education.

Reynolds, J. M. (2011). *An introduction to applied and environmental geophysics*. Hoboken: John Wiley and Sons.

Schultz, J. J., and Martin, M. M. (2012). Monitoring controlled graves representing common burial scenarios with ground penetrating radar. *J. Appl. Geophys.* 83, 74–89. doi:10.1016/j.jappgeo.2012.05.006

Steven, A., David, F., and Ginger, B. (2010). GPR characterization of a lacustrine UXO site. *Geophysics* 75, WA221–WA239. doi:10.1190/1.3467782

Van Dam, R. L., Hendrickx, J. M. H., Cassidy, N. J., North, R. E., Dogan, M., and Borchers, B. (2013). Effects of magnetite on high-frequency ground-penetrating radar. *Geophysics* 78, H1–H11. doi:10.1190/geo2012-0266.1

Virieux, J., and Madariaga, R. (1982). Dynamic faulting studied by a finite difference method. *Bull. Seismol. Soc. Am.* 72, 345–369. doi:10.1785/bssa0720020345

Warren, C., Giannopoulos, A., and Giannakis, I. (2016). gprMax: open source software to simulate electromagnetic wave propagation for ground penetrating radar. *Comput. Phys. Commun.* 209, 163–170. doi:10.1016/j.cpc.2016.08.020

Woodward, J., and Burke, M. J. (2007). Applications of ground-penetrating radar to glacial and frozen materials. *J. Environ. Eng. Geophys.* 12, 69–85. doi:10.2113/jeeg12.1.69

Xiao, T., Xiangyu, H., Cheng, L., Tao, S., Guangjie, W., Bo, Y., et al. (2022). The effects of magnetic susceptibility on controlled-source audio-frequency magnetotellurics. *Pure Appl. Geophys.* 179, 1–23. doi:10.1007/s00024-022-03050-8

Yee, K. (1966). Numerical solution of initial boundary value problems involving maxwell's equations in isotropic media. *IEEE Trans. Antennas Propag.* 14, 302–307. doi:10.1109/tap.1966.1138693

Zhou, D., and Zhu, H. (2021). Application of ground penetrating radar in detecting deeply embedded reinforcing bars in pile foundation. *Adv. Civ. Eng.* 2021, 1–13. doi:10.1155/2021/4813415

Zhou, L., Yu, D., Wang, Z., and Wang, X. (2019). Soil water content estimation using high-frequency ground penetrating radar. *Water* 11, 1036. doi:10.3390/w11051036